Nuclear Inst. and Methods in Physics Research, A 941 (2019) 162329

Contents lists available at ScienceDirect

Nuclear Inst. and Methods in Physics Research, A

journal homepage: www.elsevier.com/locate/nima

Evaluation of CsI(Na) rod scintillator application in industrial gamma-ray computed tomography

Mojtaba Askari [a], Ali Taheri [a,*], Majid Mojtahedzadeh Larijani [b], Amir Movafeghi [c], Heidar Faripour [d]

[a] Radiation Applications Research School, Nuclear Science and Technology Research Institute, Tehran, Iran
[b] Physics and Accelerators Research School, Nuclear Science and Technology Research Institute, Tehran, Iran
[c] Reactor and Nuclear Safety Research School, Nuclear Science and Technology Research Institute, Tehran, Iran
[d] Photons and Quantum Technologies Research School, Nuclear Science and Technology Research Institute, Tehran, Iran

ARTICLE INFO

Keywords:
Industrial computed tomography
Gamma-ray
CsI(Na)
Rod scintillator
Image reconstruction

ABSTRACT

The objective of this paper was to investigate a detection system based on a CsI(Na) rod scintillator for the use in industrial gamma-ray computed tomography. For this goal to be achieved, a CsI(Na) rod scintillator was first grown using the Czochralski method. The scintillation response of the rod scintillator was then assessed. Furthermore, the detection system was employed to determine the positions and energies of incident gamma-rays in a tomography system. Two different phantoms were also constructed to assess the basic characteristics of the system. Results showed that the proposed tomography system has a good performance in industrial applications.

1. Introduction

Computed Tomography (CT) is an advanced method for scanning the internal structure of objects and the demand for this method continues to rise. The first use of the CT as a non-destructive testing method in industrial applications dates back to early 1980s [1].

The CT has currently many applications such as in chemical reactor processes [2–5], bubble columns [6–8], geological studies [9,10], multiphase systems [11,12], metrology and CMM [13–15], and nondestructive testing in distillation towers [16,17].

The CT systems can entail different types of radiation sources and detectors. The radiation source employed in these systems is either a radioisotope or an X-ray generator [18,19]. In a large-scale industrial CT, the objects normally have a high density and also large dimensions and they need gamma or X-rays with higher energies in order to scan the objects [20]. The Gamma CT is a type of tomography that uses gamma radiation sources such as Am-241 for small objects and Cs-137 and Co-60 for large objects [21].

Many different types of detectors can be employed in a gamma CT, depending on the energy of gamma-rays, the response time, and the work environment. Xin et al. used 17 pairs of equidistant CZT detector elements to work on a gamma CT from incomplete projections [22]. Al-Juwaya et al. investigated the cross-sectional gas-solid distributions in spouted beds using 15 NaI (Tl) detectors [23]. Acharya et al. employed 32 BGO scintillators to carry out a performance evaluation of a cold flow catalytic column [5]. The use of scintillator arrays is common in these systems, but their relatively high costs as well as the need for complex electronics are major drawbacks. The aim of this research is to substitute rod scintillator detectors for array detectors in the cases where there is no need for high spatial resolutions. For this reason, our previous work was dedicated to proposing a new gamma CT in which a tomography setup involving a rod scintillator was simulated in order to study the characteristics of the system [24].

This work aims to experimentally implement the previously simulated setup. To that end, a rod shaped CsI(Na) crystal was first grown using the Czochralski method [25], and then polished, wrapped in an Al-Mylar acting as the reflector, and finally coupled to two PMTs, each at one end. By employing this setup, the energy spectrum and interaction position of the incident photons can be determined using a coincidence circuit. Cross sectional images of two different designed phantoms have been reconstructed to obtain the basic parameters of the system.

2. Materials and methods

2.1. Theory

There are many ways to calculate the position of the incident radiation in one dimensional scintillator detectors [24,26–28]. The basic phenomenon underlying the detector's performance is the attenuation of the light traveling along the rod scintillator length. When the

* Corresponding author.
E-mail address: atahery@aeoi.org.ir (A. Taheri).

https://doi.org/10.1016/j.nima.2019.06.070
Received 16 February 2019; Received in revised form 26 June 2019; Accepted 29 June 2019
Available online 5 July 2019

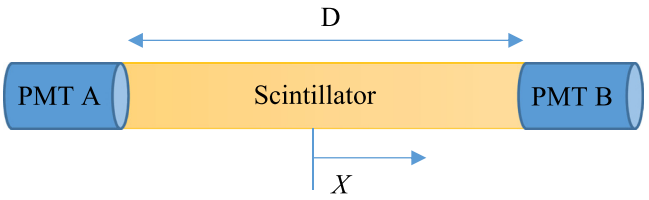

Fig. 1. A schematic view of the designed position sensitive detector setup.

gamma-rays interact with scintillator, light quanta are produced. As the Light passes through the scintillator, it is attenuated according to the light attenuation coefficient of the medium. The designed detector setup is schematically shown in Fig. 1.

In the setup shown in Fig. 1, the intensities of the PMTs' signals (S_A and S_B) are given by the following equations [29]:

$$S_A = \frac{E_\gamma P}{E_0} \exp[-\alpha(\frac{D}{2} + X)] \quad (1)$$

$$S_B = \frac{E_\gamma P}{E_0} \exp[-\alpha(\frac{D}{2} - X)] \quad (2)$$

where Eγ is the energy deposited by the gamma-ray (MeV), P is the probability that a light quantum produced at one side generates photoelectron at the other side, E_0 is the energy needed to produce a light quantum (MeV) and α is the light attenuation coefficient of the scintillator (cm^{-1}).

Energy of the gamma-rays can be calculated by multiplying Eq. (1) by Eq. (2) as follows:

$$E_\gamma = \sqrt{S_A S_B}\frac{E_0}{P} \exp\left(\alpha\frac{D}{2}\right) \quad (3)$$

Moreover, the position of the interaction between the gamma-ray and the scintillator can be calculated through dividing Eq. (2) by Eq. (1), as follows:

$$X = \frac{1}{2\alpha} \ln \frac{S_B}{S_A} \quad (4)$$

2.2. Crystal growth

The Czochralski method was used to grow the CsI(Na) crystal [25].

Considering that the maximum permissible temperature of the crucible in our crystal growth system was limited to 750 °C, so it was only possible to grow CsI(Na), CsI(Tl) and NaI(Tl) using this setup. The use of thallium dopant makes the growth process more complicated due to its evaporation, and thereby causes non-uniformity in the luminescence response of the grown crystal. The PMT used in the measurement setup had a bialkali photocathode and therefore its maximum sensitivity

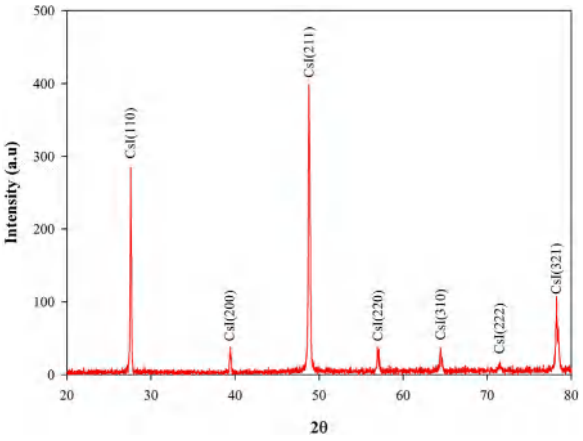

Fig. 3. XRD pattern of the grown CsI(Na) crystal.

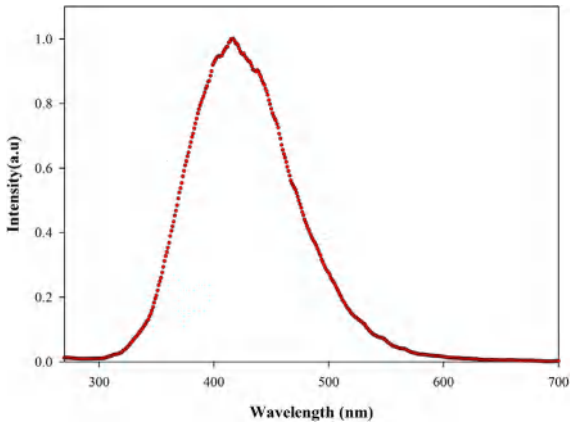

Fig. 4. Photoluminescence spectrum of the grown crystal.

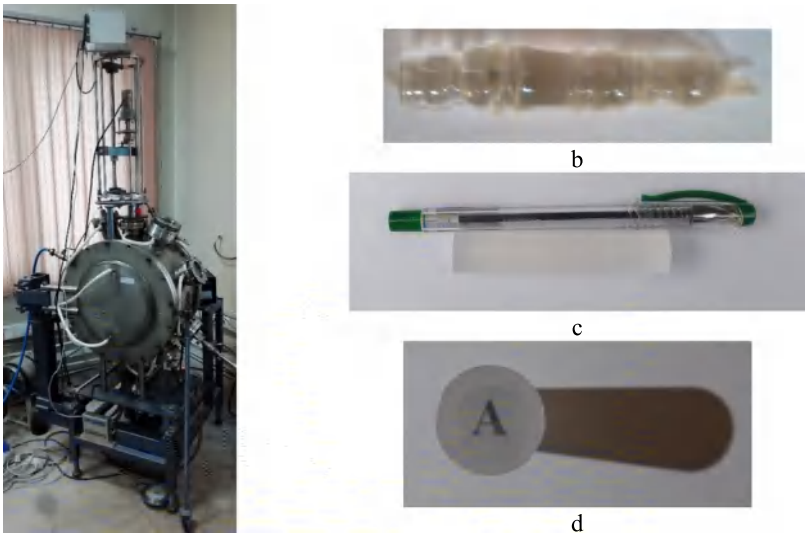

Fig. 2. Czochralski crystal growth system (a), raw crystal (b) polished crystal (c) transparency and uniformity of the grown crystal (d).

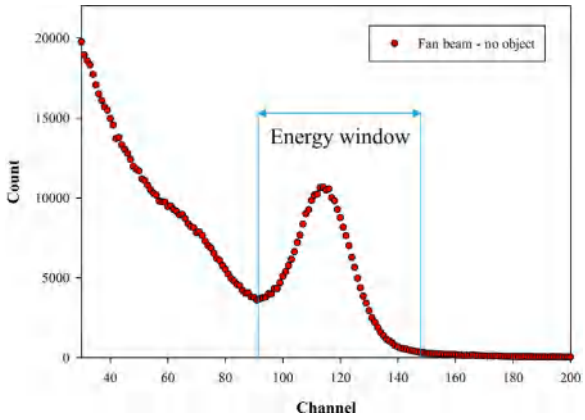

Fig. 5. Energy spectrum of the incident gamma-rays calculated by Eq. (3).

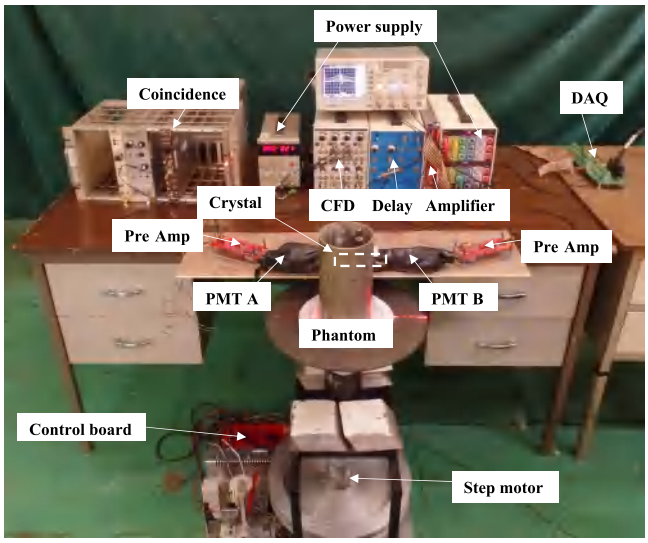

Fig. 7. Experimental setup of the computed tomography.

was at ~420 nm. Moreover, the maximum emission intensities of the CsI(Na) and NaI(Tl) were also at ~420 nm [29]. The CsI(Na) was consequently selected for crystal growth due to three main reasons including: (1) lower growing temperature, (2) lower dopant evaporation, and (3) good matching between the emission spectrum of the scintillator and the sensitivity of the employed PMTs.

In order to grow the crystal, 330 g of CsI powder with a purity of 99.99% and 0.1 g of NaI powder with a purity of 99.99% were poured into the crucible in the Czochralski crystal growth system. The powders were dried in a closed chamber and warmed up to 450 °C under vacuum.

The melt occurred under argon gas at 650 °C and 1 bar. After a short time, the molten materials reached a thermal equilibrium state. At this moment, the seed crystal which was rotating at 20 rpm and had been dipped into the melt surface was pulled from the melt surface moving at 2 mm/h.

The growth time of the crystal was about 50 h and the grown crystal was kept at a temperature of 550°C for 12 h after separation from the melt. Finally, the cooling was carried out until it reached the ambient temperature at a rate of 25 °C/h.

Fig. 2 shows the grown crystal and Czochralski crystal growth system. The length of the crystal, after turnery and polishing, was about 80 mm and its diameter was 16 mm. One of the important parameter to increase the efficiency of a scintillator is its reflector type [30,31]. In this work, Al-Mylar foil was used as the reflector and the grown scintillator was wrapped in it after polishing.

2.3. Crystal characterization

The structure of the grown crystal was characterized by X-ray diffraction (XRD). XRD spectrum of the crystal was obtained using a diffractometer (Model Stoei-stadi p) at 2θ angle as shown in Fig. 3. This spectrum shows seven peaks corresponding to the reflections from 110, 200, 211, 220, 310, 222 and 321 crystal planes (ref code: 00-001-0722).

Furthermore, photoluminescence spectrum of the crystal was obtained using a spectrophotometer (Model Varian Cary Eclipse) at 250–700 nm, as shown in Fig. 4. As the figure shows, the dominant wavelength of the emission spectrum occurs at 420 nm. This result is in agreement with that reported in the literature [32].

Fig. 5 shows the energy spectrum obtained from both of the PMTA and PMTB for Cs-137 in a fan beam geometry, while there is no phantom between the source and the detector (see Section 3.2 for more

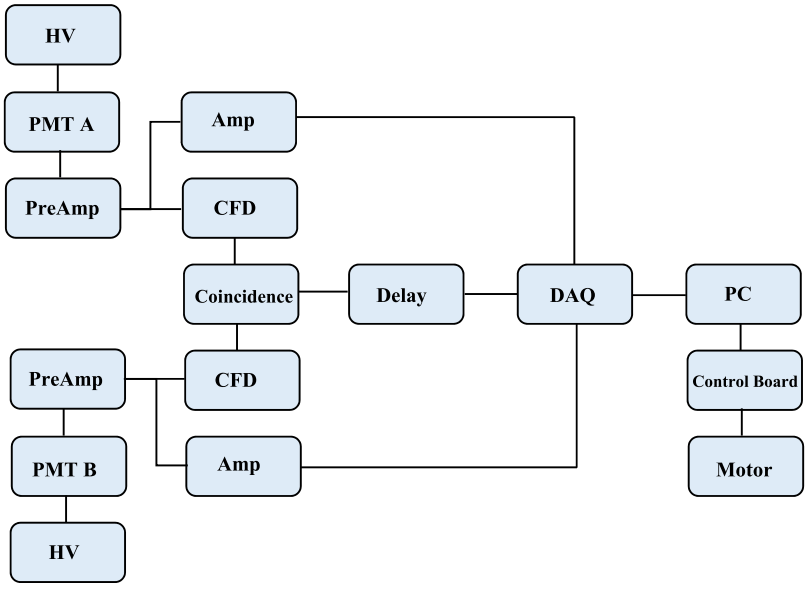

Fig. 6. Schematic view of the electronics setup for measuring the projections using the rod scintillator detector.

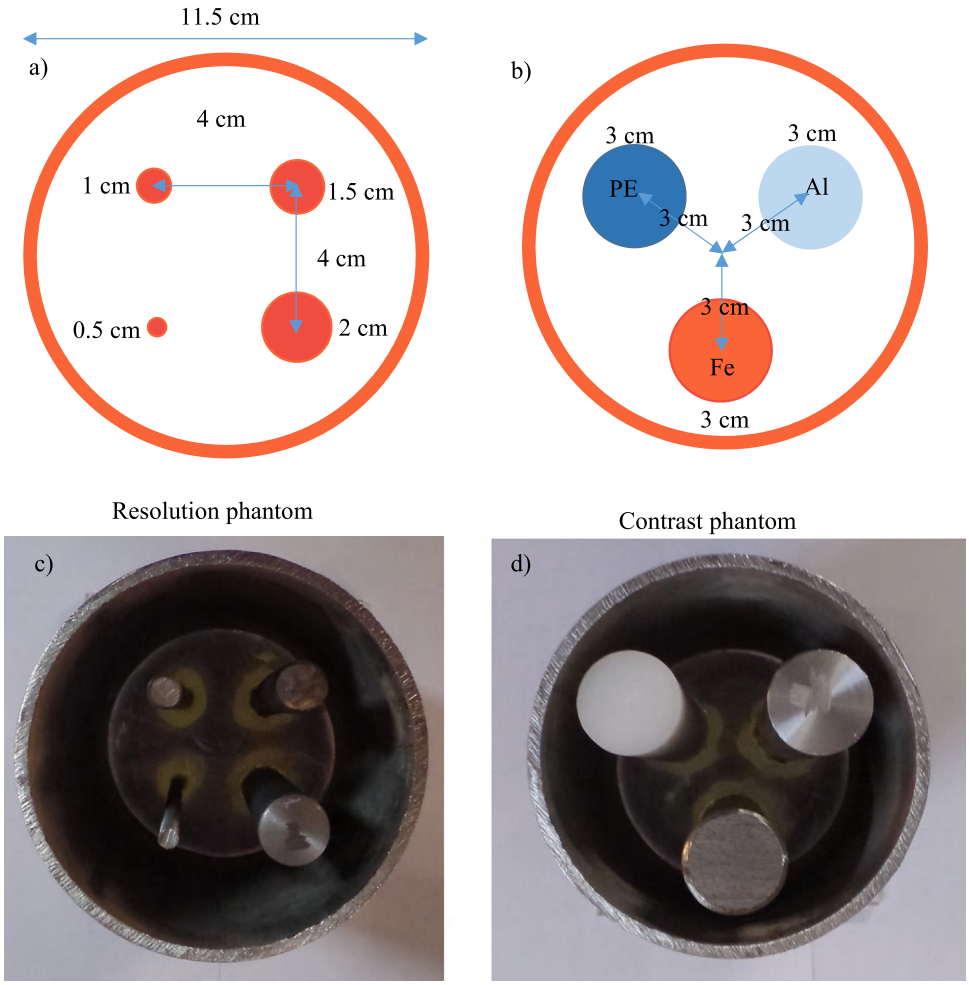

Fig. 8. The contrast and resolution phantoms; schematics (a and b) and fabricated ones (c and d).

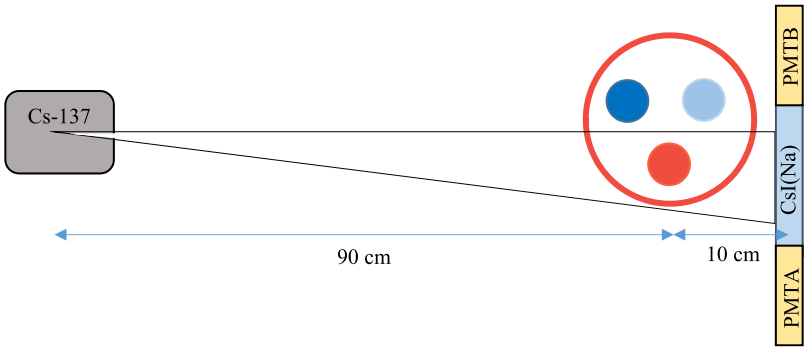

Fig. 9. Schematic top view of the tomography setup.

information). The output signals of the two PMTs are simultaneously used to obtain energy channel of the incident rays according to Eq. (3). In this case, the number of coincidences recorded for each channel is equal to the number of counts shown in the vertical axis of the histogram. The energy resolution of the recorded photopeak was obtained equal to 22.8%.

Energy resolution of a scintillation detector depends on different parameters including: (1) the intrinsic energy resolution of the crystal (a scintillator with a higher light yield produces more optical photons in each interaction of the gamma-rays and this reduces the statistical fluctuation of the PMT's output. Furthermore, the presence of impurity which reduces the transparency of the crystal can effectively increase the optical absorption coefficient of the crystal, leading to an increase in the energy resolution), (2) the intrinsic energy resolution of the PMT, (3) the geometry of the crystal (in different crystal geometries, different numbers of the optical photons reach the PMT's window. By increasing the aspect ratio of the scintillator, the light collection efficiency and the energy resolution degrade compared to a condition in which this ratio is equal 1), and (4) Optical properties of the reflector which can affect the energy resolution (as the crystal reflectivity increases, the energy resolution improves and vice versa).

As mentioned above, the obtained energy resolution of the detector depends on several parameters, mainly on the high aspect ratio of the crystal which is about 5, the reflectance of the reflector which is equal to about 70%, and the light absorption coefficient of the crystal.

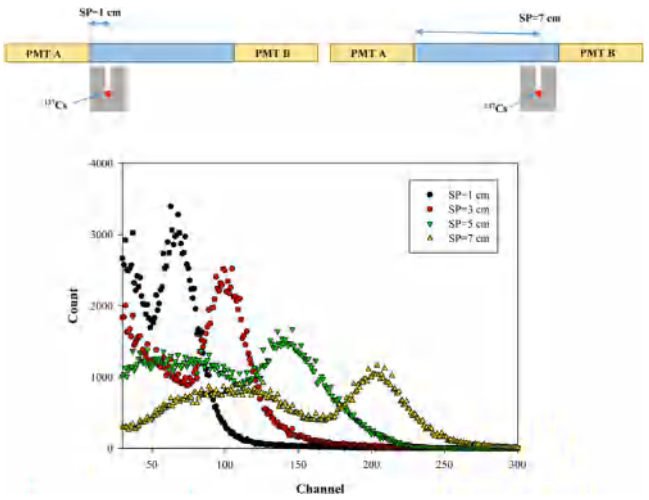

Fig. 10. The recorded gamma spectra using the PMTB when a pencil beam of Cs-137 interacts at different positions in the detector. SP is the distance between the incident position of the pencil beam and the PMTA window.

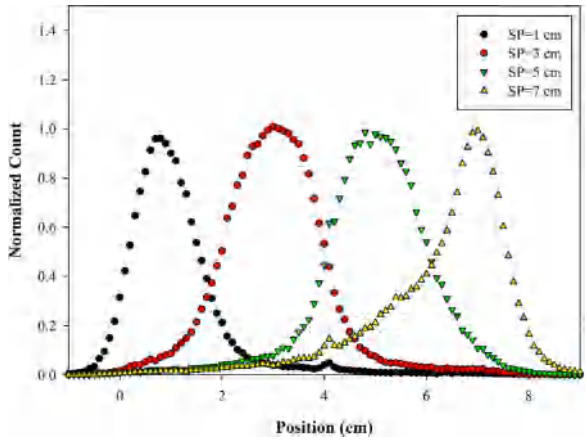

Fig. 11. Calculated positions of the incident gamma-rays from a pencil beam gamma-ray source to the detector. SP is the distance between the incident position of the pencil beam and the PMTA window.

2.4. Readout electronics

As mentioned before, each end of the rod scintillator was coupled to a PMT. When a gamma-ray interacts with the scintillator, the PMTs convert the produced scintillation light to an electronic signal. Recording the simultaneous PMTs' signals plays a significant role in obtaining the position of the interaction between the gamma-ray and the scintillator. For this reason, a coincidence system was used to record the simultaneous signals.

The readout electronics consisted of two parts: (a) a coincidence system, and (b) a pulse recorder. The output pulses of each PMT were first transmitted to a preamplifier for impedance matching. Thereafter the signal was divided into two branches; the signal of one branch was transmitted to Constant Fraction Discriminator (CFD) and then to the coincidence module to produce the trigger signal, and the signal of the second branch was transmitted to the amplifier and then to the data acquisition card. Because the CFDs use Pre-Amp output signals without any shaping, the coincidence output signal had to be transferred to a delay circuit to be synchronized with the amplified signals. Lastly, whenever there were two PMTs' signals recorded at the same time (in a pre-defined time interval), the amplified signal would be stored on the computer.

Nuclear electronics consisted of two PMTs (1 inch head on, Beijing Hamamatsu), a universal coincidence (Ortec, model 418a), a spectroscopy amplifier (Caen 16 channels, model N568Lc), a data acquisition card (model PD2-MFS-8-2M/14), and a CFD (NSTRI). A schematic view of the electronics setup is shown in Fig. 6.

The detector was coupled to the PMT with the optical pads on its both sides. After coupling, the responses of the two PMTs were matched by changing the high voltage of the PMTs and the gain of the amplifiers. In addition, the use of coincidence circuit will reduce the effect of signal distortion by comparing output of two PMTs. For example, if the shape and time characterization of the signals were changed due to the signal distortion, the coincidence circuit eliminates that event automatically.

2.5. Rotation mechanism

Obtaining projections at different angles required the object to rotate at different angles. To that end, a stepper motor (MOON) with a gearbox was employed. To automatically turn the motor on and off, a control board based on an ARM microcontroller was made, which could be controlled via a software. To obtain the angle of each position, an encoder was used. Fig. 7 shows the readout electronics and the rotation system.

2.6. Geometry and phantom

Two phantoms were used for the assessment of the resolution and contrast of the system. The resolution phantom consisted of a steel pipe, inside which were installed four parallel iron rods with diameters of 0.5, 1, 1.5 and 2 cm, respectively. The distances between the centers of the rods along the axes of x and y were 4 cm. The outer diameter and the wall thickness of the pipe were 11.5 cm and 0.4 cm, respectively, and its height was 20 cm (Figs. 8a, 8c). The contrast phantom consisted of three iron, aluminum, and polyethylene rods; each having a diameter of 3 cm, and being placed inside a steel pipe. The center of each rod was 3 cm from the phantom center (Figs. 8b, 8d).

The detector length and the phantom diameter were 8 cm and 11.5 cm, respectively, therefore the half of the projections was obtained by scanning the phantom at the angles of 0 to 180 degrees directly and the rest of the projections was obtained by reversing the *pixel numbers* (Section 3.2) while scanning the object at the angles of 180 to 360 degrees. The geometry is shown in Fig. 9.

2.7. Image reconstruction

Image reconstruction algorithms were used to reconstruct cross-sectional images using projections obtained from the detection system. The image reconstruction algorithms are generally divided into two major groups of iterative and analytical methods [33]. The analytical methods have simplified physics and standard geometry and do not include statistical models, thus they are fast and their software implementation is simple. These methods are usually used when the count rate in the detector is high like the X-ray CT. In the case of the iterative methods, statistical and physical models are considered and the noise in the reconstructed image is low. Furthermore, in these methods, the geometry can be non-standard. The disadvantages of the iterative methods are large computational times and in the case of non-standard geometries, the need for system matrix calculation [34,35].

In an industrial gamma CT, the iterative algorithms show better performance because: (1) Intensity of the radiation in a gamma CT is lower than that of a X-CT, (2) gamma-rays usually pass through high density materials like iron, therefore the count rate in the detector is lower compared to a X-CT, and (3) the larger objects have usually nonstandard geometries [36].

In our previous work, different types of iterative image reconstruction algorithm were compared, and as result it was shown that MLEM algorithms had better performance. So, in this work we used MLEM

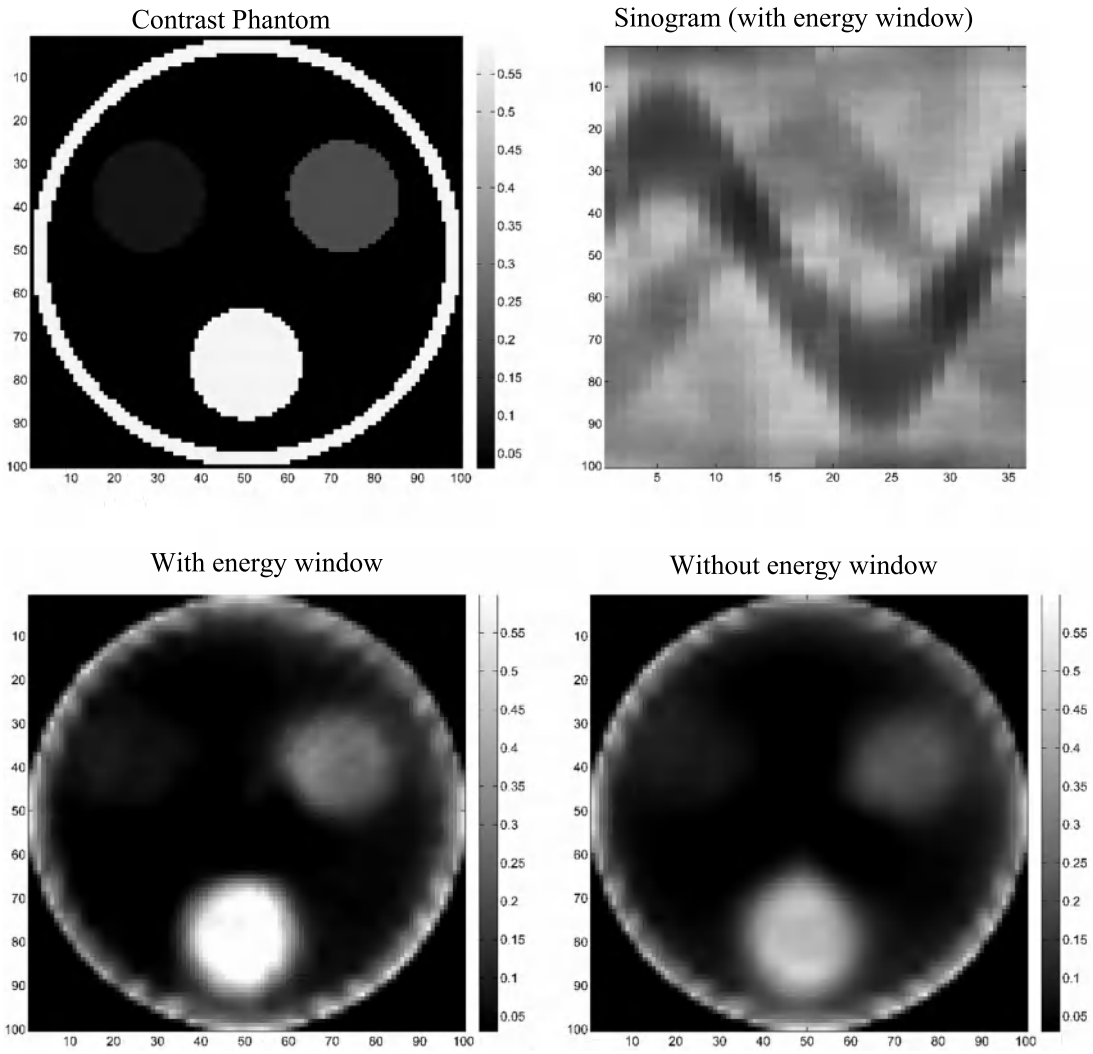

Fig. 12. Reconstructed images of the contrast phantom.

algorithm for image reconstruction [24]. Image reconstructions were done using a Matlab code written at home based on the algorithm introduced in [33].

The root mean square error was defined for comparing the reconstructed value with phantom value, as the following equation:

$$RMSE = \sqrt{\frac{\sum_j (\mu_j^{reconstruct} - \mu_j^{real})^2}{N_p}} \tag{5}$$

In order to investigate the reconstructed image, the contrast has been defined as the following equation [36,37]

$$Contrast(A, B) = \frac{|A - B|}{A + B} \tag{6}$$

where, A and B denote the average pixel values in the materials A and B, respectively.

3. Results and discussion

3.1. Evaluation of the rod scintillator

As mentioned before, the scintillation light is attenuated along the scintillator. In a rod scintillator, the attenuation varies according to the interaction point of the gamma-rays. To assess the amount of attenuation, a pencil beam gamma source was placed at different positions in front of the detector and the associated gamma spectra were recorded using the PMTB as shown in Fig. 10. The pencil beam was implemented using a lead collimator having a hole with a radius of 2 mm. As can be seen from Fig. 10, the signal height increases by decreasing the source to PMT distance and vice versa. The differences between the pulse heights can be used to determine the position of the interaction in a rod shaped scintillator.

Fig 11 shows the calculated interaction positions using Eq. (4). As shown in Fig. 11, the scintillator can act as a position sensitive detector for the incident gamma-rays.

The relatively low energy resolution of the detector is directly dependent on the quality and dimensions of the crystal. Improving the quality of the crystal will definitely increase the energy and spatial resolutions of the system, but this increase will not be dramatic. We discussed about employing high aspect ratio scintillators for tomography purposes in [24] where a NaI(Tl) rod scintillator with a good quality was simulated and the results showed that this type of tomography system has a spatial resolution on the order of centimeters.

After calculating the interaction position of the gamma-rays, it was necessary to set a suitable energy window for the recorded gamma-rays' energies in order to achieve low noise images. The energy window is shown Fig. 5.

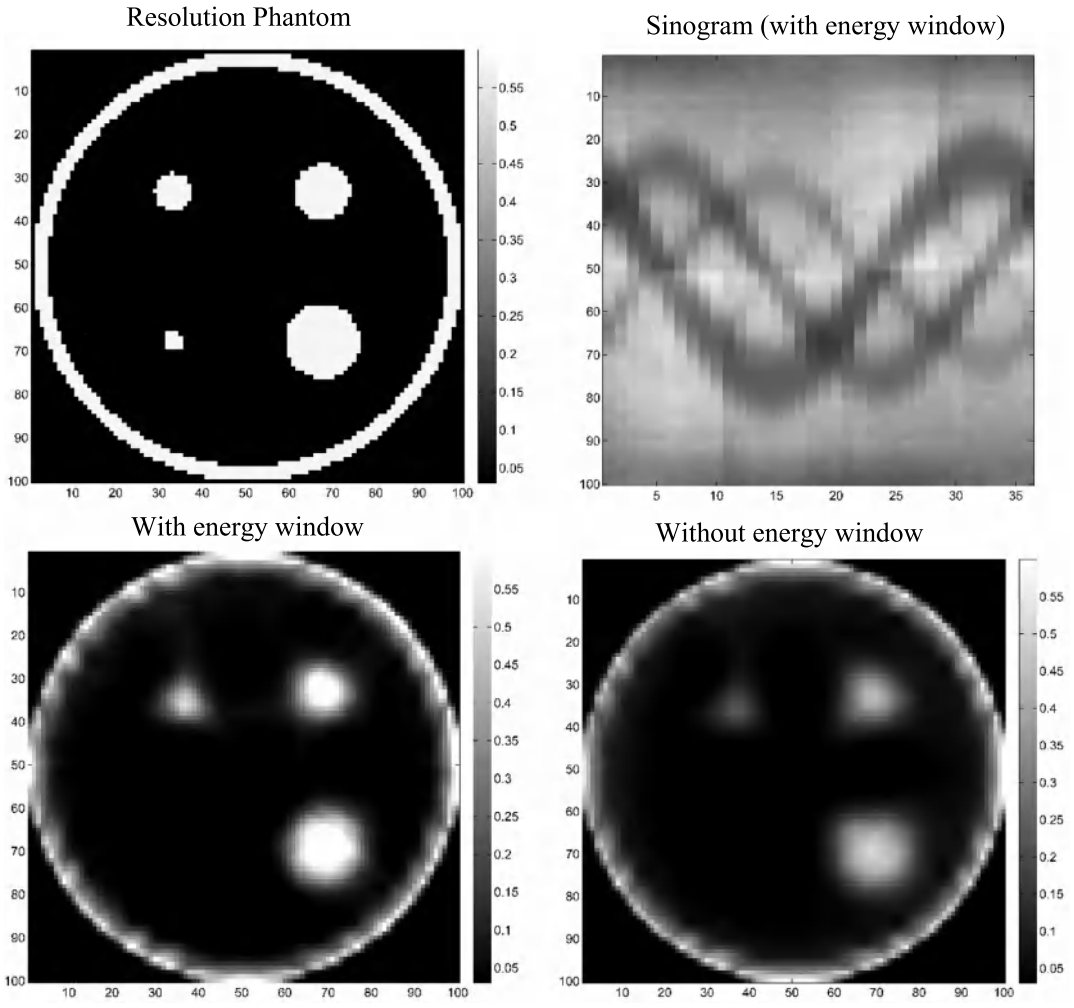

Fig. 13. Reconstructed images of the resolution phantom.

3.2. Computed tomography

In a CT scan of an object, different projections at different angles are needed to reconstruct its cross sectional image. For obtaining these projections, the detector is divided into several virtual pixels. After measuring the gamma-rays' energies, an energy window was applied to eliminate the scattered gamma-rays. The phantoms described in Section 2.5 are placed between a Cs-137 gamma-ray source with an activity of 3.4 mCi and the detector. Each projection is recorded in a counting time of 5 min. The phantoms are rotated from 0 to 360 degrees in steps of 10 degrees. After obtaining the projections, the cross sectional image of the phantoms are reconstructed using MLEM algorithm with 30 iterations. It is important to note that because of using a low thickness detector in one dimension, it is only possible to perform one slice tomography using the proposed system.

Fig. 12 shows the contrast phantom, its reconstructed images with and without the energy window and the associated sinogram. As the figure shows, the reconstructed image without the energy window was more blurred than the one where the energy window was considered. The contrast is defined according to Eq. (6) as the ratio of the three different material intensities of the contrast phantom. The contrast and root mean square error are presented in Table 1.

Based on the results of Table 1, when the energy window is limited to the photo-peak energy, the contrast improves and the associated error decreases.

Fig. 13 shows the resolution phantom, the reconstructed images of this phantom and the relevant sinogram. As shown in this figure, applying the energy window resulted in a sharper image. The iron rod with the smallest diameter of 0.5 cm is not distinctly visible in the reconstructed images, showing that the system resolution can be from 0.5 to 1 cm. The RMSEs for the resolution phantom, with and without the energy window, were obtained to be 0.1351 and 0.1404, respectively.

Table 1
Calculated contrasts of the system with and without applying the energy window.

	Contrast (Fe, Al)	Contrast (Fe, PE)	Contrast (Al, PE)	RMSE
With energy window	0.36	0.78	0.58	0.137
Without energy window	0.35	0.69	0.44	0.141

As mentioned in the introduction, there are different types of industrial gamma-ray tomography systems. The spatial resolutions of these systems depend on characterizations of the detector, geometry of the system, number of the projections, reconstruction algorithm, and radiation source specifications [38]. Based on the literature, the spatial resolution of a gamma-ray tomography system is from 2.5 mm to 19 mm [22,23,39,40] and therefore the resolution of our proposed system falls within this range.

4. Conclusion

In this paper, the performance of a CsI(Na) rod scintillator detector in gamma tomography systems was studied. A rod scintillator

was grown by the Czochralski method. In the first step, the detector response was obtained by placing the radiation source at different positions in front of the detector. In the second and final steps, the developed detector was employed in an industrial computed tomography system and the resolution and the contrast of the system were determined. The resolution of the system was estimated to be about 1 cm and iron to polyethylene contrast was obtained 0.78. This investigation constituted the conclusion that rod scintillator detectors can be used in computed tomography systems for applications that do not require high precisions. Future researches can be dedicated to enhancing the position sensitivity of the rod scintillator detectors.

References

[1] A. Cantatore, P. Müller, Introduction to Computed Tomography, DTU Mechanical, 2011.
[2] D.V. Kalaga, A.V. Kulkarni, R. Acharya, U. Kumar, G. Singh, Some industrial applications of gamma-ray tomography, J. Taiwan Inst. Chem. Eng. 40 (6) (2009) 602–612.
[3] A. Cantatore, P. Müller, Introduction to Computed Tomography, Kgs.Lyngby: DTU Mechanical Engineering, 2011.
[4] W.A. Kalender, X-ray computed tomography, Phys. Med. Biol. 51 (13) (2006) 29–43.
[5] R. Acharya, L. Y., U. Kumar, V. Patankar, S. Kar, A. Dash, Performance evaluation of process tomography system for cold flow catalytic column, Chem. Eng. Res. Des. (2017).
[6] A. Kemoun, B.C. Ong, P. Gupta, M.H. Al-Dahhan, M.P. Dudukovic, Gas holdup in bubble columns at elevated pressure via computed tomography, Int. J. Multiph. Flow. 27 (5) (2001) 929–946.
[7] U.P. Veera, Gamma ray tomography design for the measurement of hold-up profiles in two-phase bubble columns, Chem. Eng. J. 81 (1–3) (2001) 251–260.
[8] A.J. Sultan, L.S. Sabri, M.H. Al-Dahhan, Impact of heat-exchanging tube configurations on the gas holdup distribution in bubble columns using gamma-ray computed tomography, Int. J. Multiphase Flow (2018).
[9] L.F. Pires, O.O. Bacchi, K. Reichardt, Gamma ray computed tomography to evaluate wetting/drying soil structure changes, Nucl. Instrum. Methods Phys. Res. B 229 (3–4) (2005) 443–456.
[10] L.F. Pires, J.A. Borges, O.O. Bacchi, K. Reichardt, Twenty-five years of computed tomography in soil physics: A literature review of the Brazilian contribution, Soil Tillage Res. 110 (2) (2010) 197–210.
[11] A. Bieberle, H. Nehring, R. Berger, M. Arlit, H.-U. Härting, M. Schubert, U. Hampel, Compact high-resolution gamma-ray computed tomography system for multiphase flow studies, Rev. Sci. Instrum. 84 (3) (2013).
[12] I. Ismail, J. Gamio, S. Bukhari, W. Yang, Tomography for multi-phase flow measurement in the oil industry, Flow Measur. Instrum. 16 (2–3) (2005) 145–155.
[13] R. Adamsa, R. Zborayb, Gamma radiography and tomography with a CCD camera and Co-60 source, Appl. Radiat. Isot. 127 (2017) 22–26.
[14] J. Kruth, M. Bartscher, S. Carmignato, R. Schmitt, L.D. Chiffre, A. Weckenmann, Computed tomography for dimensional metrology, CIRP Ann. Manuf. Technol. 60 (2) (2011) 821–842.
[15] S. Carmignato, W. Dewulf, R. Leach, Industrial X-Ray Computed Tomography, Springer, 2018.
[16] M. Khorsandi, S.A.H. Feghhi, Gamma-ray CT as a complementary technique for structural inspection of tray-type distillation columns, Measurement 78 (2016) 1–8.
[17] M.K. Al Mesfer, A.J. Sultan, M.H. Al-Dahhan, Impacts of dense heat exchanging internals on gas holdup cross-sectional distributions and profiles of bubble column using gamma ray Computed Tomography (CT) for FT synthesis, Chem. Eng. J. 300 (2016) 317–333.
[18] M. Wang, Industrial Tomography Systems and Applications, Woodhead Publishing, Cambridge, 2015.
[19] S. Carmignato, W. Dewulf, R. Leach, Industrial X-Ray Computed Tomography, springer, 2018.
[20] A. Velo, M. Hamada, D. Carvalho, J. Martins, C. Mesquita, A portable tomography system with seventy detectors and five gamma-ray sources in fan beam geometry simulated by Monte Carlo method, Flow Measur. Instrum. (2016).
[21] IAEA-TECDOC-1589, Industrial Process Gamma Tomography, International Atomic Energy Agency, Vienna, 2008.
[22] S. Xin, H.X. Wang, Gamma-ray CT from incomplete projections for two-phase pipe flow, Rev. Sci. Instrum. 18 (2) (2017).
[23] T. Al-Juwaya, N. Ali, M. Al-Dahhan, Investigation of cross-sectional gas-solid distributions in spouted beds using advanced non-invasive gamma-ray computed tomography (CT), Exp. Therm Fluid Sci. 86 (2017) 37–53.
[24] M. Askari, A. Taheri, M.M. larijani, A. Movafeghi, Industrial gamma computed tomography using high aspect ratio scintillator detectors (A Geant4 simulation), Nucl. Instrum. Methods Phys. Res. A 923 (2019) 109–117.
[25] H.J. Scheel, T. Fukuda, Crystal Growth Technology, John Wiley & Sons, 2004.
[26] A. Taheri, R. Peyvandi, M. Sasanpour, M. Askari, Spectral response evaluation of plastic rod scintillators as position sensitive beta particle detector, J. Instrum. 10 (12) (2015).
[27] R. Peyvandi, A. Taheri, M. Lehdarboni, Evaluation of a new position sensitive detector based on the plastic rod scintillators, J. Instrum. 10 (6) (2015).
[28] M. Askari, M.A. Mirzahasanlou, M.T. Sasanpour, A. Taheri, Position estimation of a gamma-ray source using NaI-plastic combined detectors, J. Instrum. 13 (7) (2018).
[29] G.F. Knoll, Radiation Detection and Measurement, Wiley, New York, 2010.
[30] M. Askari, A. Taheri, M.T. Sasanpour, Measurement of effective optical reflectivity using gamma ray spectroscopy method, Optik (2018) http://dx.doi.org/10.1016/j.ijleo.2018.02.093.
[31] A. Taheri, M. Askari, M.T. Sasanpour, Lead foil wrapping of the plastic scintillators for the gamma ray detection: optical reflector or spectrum intensifier? J. Instrum. 12 (08) (2017).
[32] D.W. Aitken, B.L. Beron, G. Yenicay, H.R. Zulliger, The fluorescent response of NaI(Tl), CsI(Tl), CsI(Na) and CaF2(Eu) to X-rays and low energy gamma rays, IEEE Trans. Nucl. Sci. 14 (1) (1967) 468–477.
[33] G.L. Zeng, Medical Image Reconstruction, Springer, USA, 2010.
[34] K. Lange, M. Bahn, R. Little, A theoretical study of some maximum likelihood algorithms for emission and transmission tomography, IEEE Trans. Med. Imaging 6 (2) (1987) 106–114.
[35] J. Kim, S.-h. Jung, J. Moon, J. Guen Park, J. Jin, G. Cho, Development of transportable gamma-ray tomographic system for industrial application, Nucl. Instrum. Methods Phys. Res. A 693 (2011) 203–208.
[36] M. Khorsandi, S. Feghhi, Development of image reconstruction for gamma-ray CT of large-dimension industrial plants using Monte Carlo simulation, Nucl. Instrum. Methods Phys. Res. B 356–357 (2015) 176–185.
[37] C. Kamphuis, F. Beekman, Accelerated iterative transmission CT reconstruction using an ordered subsets convex algorithm, IEEE Trans. Med. Imaging 17 (6) (1998) 1101–1105.
[38] L. De Chiffre, S. Carmignato, J.-P. Kruth, R. Schmitt, A. Weckenmann, Industrial applications of computed tomography, Int Acad Prod. Eng. 63 (2) (2014) 655–677.
[39] C.H. d. Mesquita, A.F. Velo, D.V.S. Carvalho, J.F.T. Martins, M.M. Hamada, Industrial tomography using three different gamma ray energies simultaneously - image analysis, Flow Measur. Instrum. (2015).
[40] J. Abdullah, H. Hassan, M.R. Shari, S. Mohd, M. Mustapha, A.A. Mahmood, S. Jamaludin, M.R. Ngah, N.H. Hamid, GammaScorpion: mobile gamma-ray tomography system for early detection of basal stem rot in oil palm plantations, Opt. Eng. 52 (3) (2013) 12.